Proton movement and coupling in the POT family of peptide transporters

Joanne L. Parker[a,1], Chenghan Li[b,c,d], Allete Brinth[e,f], Zhi Wang[b,c,d], Lutz Vogeley[e,f], Nicolae Solcan[a], Gregory Ledderboge-Vucinic[a], Jessica M. J. Swanson[b,c,d,1], Martin Caffrey[e,f], Gregory A. Voth[b,c,d], and Simon Newstead[a,1]

[a]Department of Biochemistry, University of Oxford, Oxford OX1 3QU, United Kingdom; [b]Department of Chemistry, The University of Chicago, Chicago, IL 60637; [c]Institute for Biophysical Dynamics, The University of Chicago, Chicago, IL 60637; [d]James Franck Institute, The University of Chicago, Chicago, IL 60637; [e]School of Medicine, Trinity College Dublin, Dublin, Ireland; and [f]School of Biochemistry and Immunology, Trinity College Dublin, Dublin, Ireland

Edited by Christopher Miller, Howard Hughes Medical Institute, Brandeis University, Waltham, MA, and approved November 3, 2017 (received for review June 25, 2017)

POT transporters represent an evolutionarily well-conserved family of proton-coupled transport systems in biology. An unusual feature of the family is their ability to couple the transport of chemically diverse ligands to an inwardly directed proton electrochemical gradient. For example, in mammals, fungi, and bacteria they are predominantly peptide transporters, whereas in plants the family has diverged to recognize nitrate, plant defense compounds, and hormones. Although recent structural and biochemical studies have identified conserved sites of proton binding, the mechanism through which transport is coupled to proton movement remains enigmatic. Here we show that different POT transporters operate through distinct proton-coupled mechanisms through changes in the extracellular gate. A high-resolution crystal structure reveals the presence of ordered water molecules within the peptide binding site. Multiscale molecular dynamics simulations confirm proton transport occurs through these waters via Grotthuss shuttling and reveal that proton binding to the extracellular side of the transporter facilitates a reorientation from an inward- to outward-facing state. Together these results demonstrate that within the POT family multiple mechanisms of proton coupling have likely evolved in conjunction with variation of the extracellular gate.

membrane transport | biophysics | proton movement | major facilitator superfamily | peptide transport

The POT/PTR/NPF family of secondary active transporters drive the concentrative uptake of their substrates by utilizing the proton electrochemical gradient ($\Delta\mu H^+$) across the membrane (1). The POT family belong to the major facilitator superfamily (MFS) of secondary active transporters (2), which minimally contain 12 transmembrane-spanning alpha helices (TMs) arranged as two six-helix bundles in the membrane (3). Occasionally two additional helices are inserted between the two six-helix bundles, the role of which appears to aid the structural stability of these proteins (4). A remarkable feature of the family is the diversity and extent of natural substrates that are recognized. These range from short-chain di- and tripeptides in bacteria, fungi, and mammals to nitrate, glucosinolates, and hormones in plants (5). Individual members can show tight substrate selectivity; for example, the plant proton-coupled nitrate transporter NRT1.1. can recognize nitrate but not peptides (6). Some peptide transporters, however, can recognize >8,000 different di- and tripeptides, which are themselves chemically diverse (7). The variation of substrates expands further with the mammalian peptide transporters PepT1 and PepT2, which are responsible for beta lactam absorption in the small intestine and have been targeted to improve the oral bioavailability of peptide-based prodrug molecules (8, 9). Although substrate recognition between family members changes, many of the sites of putative protonation are nevertheless conserved (4). It is difficult therefore to rationalize how the POT family is able to maintain its strict coupling between proton and ligand, which is the hallmark of secondary active transporters, when their ligands vary so dramatically.

Secondary active transporters often operate through an alternating access mechanism, where conformational changes in the protein alternately expose a ligand binding site to either side of the membrane (10). Minimally this involves an outward-facing state, where the transporter can bind ligand and driving ion, transitioning to an occluded conformation, and finally an inward-facing state, where the ion and ligand dissociate into the cell (11). Reorientation of the empty carrier enables the system to reset and further transport to occur. In the POT family substrate recognition has been studied through cocrystal structures and biochemical assays, revealing that binding promiscuity is partly the result of multiple binding pockets that can accommodate peptides in different orientations (12) and can employ variable proton stoichiometry (13). However, the role of protons in ligand recognition and transport is still poorly understood, in part due to difficulties in monitoring this aspect of the transport mechanism. To date the best-studied proton-coupled transporter within the MFS is LacY, the lactose permease from *Escherichia coli* (14). Here, conformational switching between an outward-facing and inward-facing state is driven kinetically through the release of protons from the transporter on the inside of the membrane (15). Once deprotonated, LacY spontaneously transitions from

Significance

The uptake of nutrients from the environment is an essential process that is achieved in most cells through the use of secondary active transporters. The POT family of proton-coupled peptide transporters are one of the most diverse nutrient uptake systems, recognizing amino acids, peptides, nitrate, and seed-defense compounds. A long-standing question is how this family achieves such ligand diversity. A high-resolution crystal structure combined with multiscale molecular dynamics simulations demonstrate water molecules are able to shuttle protons using a Grotthuss-type mechanism, suggesting a separation of ligand recognition from proton movement. This would have clear advantages for a transporter family that must accommodate chemically diverse ligands while retaining the ability to couple transport to the proton electrochemical gradient.

Author contributions: J.L.P., J.M.J.S., M.C., G.A.V., and S.N. designed research; J.L.P., C.L., A.B., Z.W., L.V., N.S., G.L.-V., J.M.J.S., and S.N. performed research; J.L.P., C.L., and M.C. contributed new reagents/analytic tools; J.L.P., C.L., J.M.J.S., M.C., G.A.V., and S.N. analyzed data; and J.L.P., C.L., J.M.J.S., and S.N. wrote the paper.

The authors declare no conflict of interest.

This article is a PNAS Direct Submission.

Data deposition: The atomic coordinates and structure factors have been deposited in the Protein Data Bank, www.wwpdb.org (PDB ID code 6EI3).

[1]To whom correspondence may be addressed. Email: joanne.parker@bioch.ox.ac.uk, jmswanson@uchicago.edu, or simon.newstead@bioch.ox.ac.uk.

This article contains supporting information online at www.pnas.org/lookup/suppl/doi:10.1073/pnas.1710727114/-/DCSupplemental.

the inward-open to outward-open state (16). A key feature in the mechanism of LacY is the interaction between residues that link lactose recognition and proton binding, which facilitate the tight coupling in this system (17). However, it is difficult to imagine a similar mechanism operating within the POT family, as many of the sites of proton binding are conserved in members that recognize very different ligands (18).

In the POT family, transport is achieved through the movement of the gating helices around the central binding site (19). The extracellular gate, formed by TM1, 2 from the N-terminal bundle pack against TM7, 8 from the C-terminal bundle, serves to control access to the binding site from the extracellular side of the membrane. The intracellular gate is formed by TM4, 5 packing against TM10, 11 and controls the release of peptide and protons on the inside of the cell. We previously identified two salt-bridge interactions that coordinate these helices and control the conformational state of the transporter (20). However, whereas the intracellular gate contains a highly conserved lysine and glutamate pair, the extracellular gate salt bridge is much less conserved (4). In the majority of bacterial POTs the extracellular gate salt bridge is an arginine and glutamate pair, while in the mammalian members of the POT family, PepT1 and PepT2, a conserved histidine on TM2 combined with an aspartate–arginine salt bridge on TM1 and 7 is observed (21). Electrophysiology studies on human PepT1 in oocytes and HeLa cells have shown the histidine is an essential part of the transport mechanism and involved in substrate recognition (21). Intriguingly, the TM2 histidine is also found in a subset of "mammalian-like" bacterial members, including one of the proteins from the bacterium *Shewanella oneidensis*, $PepT_{So}$, where it was shown to be located at the base of an extracellular cavity in an inward-facing occluded state (22). Although recent crystal structures of bacterial POT family transporters have identified how peptide binding might disrupt these salt-bridge interactions (23–25), they have not explained how protons might move between the intracellular and the extracellular gates.

In this study we sought to understand the role of the extracellular gate histidine in the mammalian-like family members. Transport assays identify a triad of conserved residues in the extracellular gate, which are required to coordinate proton binding. A high-resolution structure of a mammalian-like bacterial POT family transporter from *Xanthomonas campestris*, $PepT_{Xc}$, at 2.1-Å resolution further revealed networks of ordered water molecules that connect key sites of proton binding. Multiscale molecular dynamics (MD) simulations reveal facile proton transport between key intracellular and extracellular residues can occur through these waters on the microsecond timescale. Our data indicate that different members of the POT family have evolved distinct mechanisms to link transport to the proton gradient, and that proton binding to the extracellular gate may drive reorientation of the transporter from inward- to outward-facing states.

Results and Discussion

Alternative Gating Mechanism. To gain further insight into the proton coupling mechanism within the mammalian-like members of the POT family we sought to identify the contributions of key sites of proton binding and release within $PepT_{So}$. Using a reconstituted transport assay we found that His61 on TM2 is essential for proton-coupled uptake, as are the other side chains of the ExxER motif on TM1 and the intracellular gate salt bridge between Glu419 on TM10 and Lys127 on TM5 (Fig. 1 *A* and *B*). Interestingly we discovered that mutating Arg32, usually part of the extracellular gate within the family (20), to an alanine resulted in a fully functional transporter, showing WT levels of transport in our proton-dependent uptake assay. This is a significant difference, given that the equivalent arginine in $PepT_{St}$ and GkPOT has been shown to be essential for proton-coupled transport and interacts with a glutamate on TM7 to stabilize the inward-open conformation (23). Another notable difference we observed in $PepT_{So}$ was its pH optimum. Previous POT family members have showed a slight difference in transport rate with regard to pH and have a pH optimal around pH 6.0–6.5 (20, 23). In contrast, $PepT_{So}$ shows a strong pH dependency, with maximal activity at more alkaline values, 7.5–8 (Fig. 1*C*). Given the differences we observed with respect to Arg32, we reasoned that this difference may be due to the introduction of the histidine at the extracellular gate. To further investigate the role of the histidine in proton coupling we mutated this residue to an aspartic acid, which has a lower pK_a (~3.5) compared with histidine (~6.5), and tested the effect of pH on transport. In other POT family transporters, the equivalent residue is often an alanine or serine (Fig. S1). We observed a new pH optimum for the His61Asp variant, which shifts toward the acidic range, with maximal transport rate at pH 6.0–6.5 (Fig. 1*C*), consistent with the lower pK_a of aspartic acid. This result highlights an important role for the TM2 histidine in the proton coupling mechanism in the mammalian-like family members and explains earlier reports on the importance of this side chain in PepT1 (26). It also provided a logical explanation for the redundancy of Arg32 in proton coupling and prompted us to consider that the introduction of the histidine in the mammalian-like members may have altered the proton coupling mechanism compared with other POT family transporters.

Previously we established that $PepT_{St}$ transports di- and tripeptides using a dual mechanism, with five to six protons being

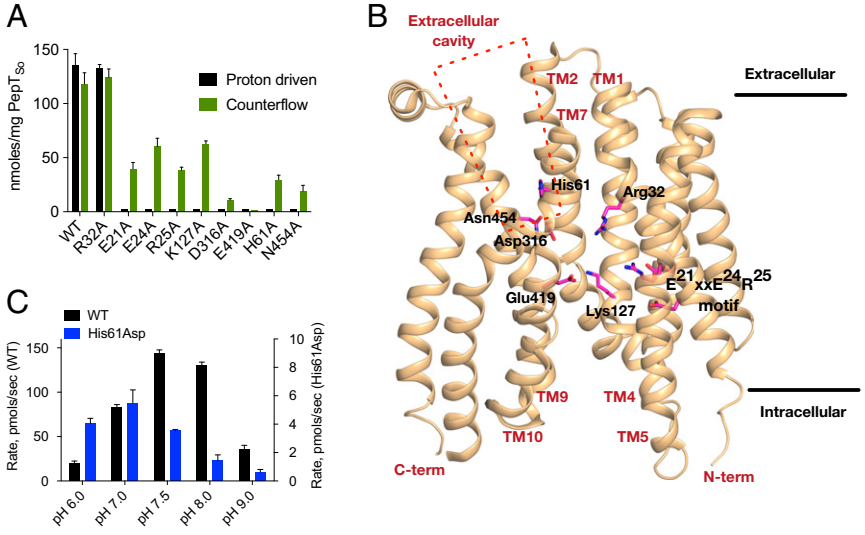

Fig. 1. Residues important for proton coupling in $PepT_{So}$. (*A*) Proton-driven and counterflow data for conserved residues in $PepT_{So}$. (*B*) Structure of $PepT_{So}$ in an inward-open conformation (PDB ID code 4UVM) indicating the location of residues involved in proton coupling and their interacting partners and highlighting the extracellular cavity leading to His61. (*C*) Rate of proton driven transport of both WT and the His61Asp variant at different pH values.

used for dipeptides and three protons for tripeptides (13). Therefore, we wanted to see if this dual transport mechanism also held true for $PepT_{So}$. We found that $PepT_{So}$ can transport a wider range of peptide substrates than $PepT_{St}$, including one of the largest natural substrates for the family, the tripeptide L-Tyr-Tyr-Tyr and the peptide prodrug valacyclovir (Fig. S2). However, attempts to calculate the number of protons required for di- or tripeptide uptake with $PepT_{So}$ were unsuccessful, as robust activity was not observed in the previously used pyranine-based assay. However, an important feature of a dual coupling stoichiometry mechanism is the amount of substrate that can be transported under steady-state conditions. For $PepT_{St}$ dipeptides, which utilize five or six protons for transport, are transported to much higher concentrations (~10 times) than tripeptides, which requires only three protons when using either ΔpH (13) or $\Delta\mu H^+$ (Fig. 2*A*). However, under steady-state transport conditions, using either ΔpH alone (Fig. 2*B*, dashed lines) to drive transport or $\Delta\mu H^+$ (Fig. 2*B*, solid lines), $PepT_{So}$ concentrated dialanine to similar levels as trialanine. This indicates that $PepT_{So}$ transports peptides of different sizes using the same mechanism, highlighting an important mechanistic difference between the non-histidine-containing peptide transporters and the histidine-containing ones.

Sequence Divergence at the Extracellular Gate. On examination of sequence alignments it becomes clear that homologs containing a histidine on TM2 always have an aspartic acid on TM7 rather than the glutamate found in non-histidine-containing POT family transporters (Fig. 3*A* and Fig. S1). The aspartic acid in $PepT_{So}$, Asp316, is clearly important for transport (Fig. 1*A*), being required for both proton-coupled and counterflow uptake. The structure shows the shorter reach of the aspartate would not allow for a strong interaction with Arg32 on TM1 (Fig. 1*B*), potentially indicating why this arginine is not required for transport in $PepT_{So}$ but is required in GkPOT and $PepT_{St}$, which both contain glutamate at this position (20, 23) (Fig. S2). Given the close positioning of the histidine on TM2 to the aspartate, we considered the potential for this histidine to replace the arginine in forming the salt bridge between the extracellular gate helices. However, the crystal structure shows that Asp316 and His61 are not interacting directly, but rather interact through Asn454. This asparagine is again conserved specifically within the histidine-containing members of the family and, like His61 and Asp316, is essential for activity (Fig. 1*B*), implying a functional coupling between this triad of residues at the apex of the peptide-binding site. To test for a possible interaction between the histidine on TM2 and aspartate on TM7 we combined our His61Asp and Asp316His variants. While both individual mutants retained activity, albeit at a much lower level than WT protein (Fig. S3), swapping the residues allowed for increased proton-coupled transport (Fig. 3*B*), supporting a functional interaction. This result suggests that within the POT family there exist two

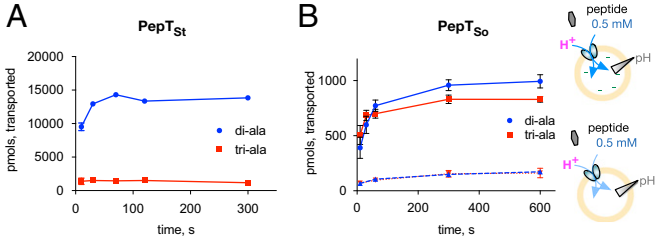

Fig. 2. $PepT_{So}$ transports both di- and trialanine using the same number of protons. Steady-state accumulation of di- and trialanine, driven using a fixed $\Delta\mu H^+$, in $PepT_{St}$ (*A*) and $PepT_{So}$ (*B*, solid lines). Dashed lines indicate the steady-state accumulation of di-and trialanine driven using ΔpH only. Schematics show the experimental setup; the gray triangle indicates a ΔpH, alkaline inside produced from an acetate diffusion gradient and – indicates a negative inside membrane potential produced through a potassium gradient.

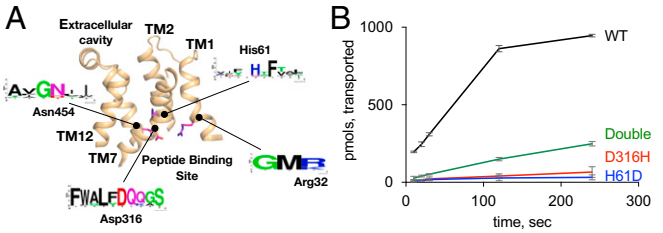

Fig. 3. Conservation of the TM2 histidine in mammalian and mammalian-like POT family transporters. (*A*) The extracellular cavity from $PepT_{So}$ (PDB ID code 4UVM) is shown with the conserved TM2 histidine, His61, and extracellular gate residues, Asp316 and Arg32. Asn454 can be seen coordinating the interaction between His61 and Asp316 in this conformation. Sequence logos show the conservation of these residues among the mammalian members of the POT family. (*B*) Proton-driven uptake of dialanine over time for His61Asp, Asp316His, and the double mutant.

mechanisms for proton coupling, one which is more mammalian-like and contains the conserved histidine and another which is more prokaryotic-like without the histidine. However, to understand further the network of interactions surrounding this conserved triad of residues and delineate potential protonation pathways within the transporter requires a higher-resolution structure than is currently available for the mammalian-like members (12). Following an extensive search of prokaryotic genomes we identified a suitable homolog from *X. campestris*, $PepT_{Xc}$ (Fig. S4). Similar to $PepT_{So}$, $PepT_{Xc}$ shares 32% sequence identity with the human PepT1 transporter and contains the equivalent configuration of residues in the extracellular gate. We succeeded in crystallizing $PepT_{Xc}$ using the *in meso* crystallization method and determined the structure to a maximum resolution of 2.1 Å (Fig. 4*A* and Table S1).

Crystal Structure of $PepT_{Xc}$. $PepT_{Xc}$ contains 14 transmembrane helices, in an arrangement similar to $PepT_{So}$ (rmsd 1.37 Å over 496 Cα atoms), with which it shares 64% identity. The structure was captured in an autoinhibited state, with the C terminus of the protein curling back on the transporter and blocking the exit of the peptide binding site (Fig. S5 *A* and *B*). The tobacco etch virus (TEV) protease recognition site (ENLYFQ) can clearly be seen in the electron density map, with the terminal glutamine interacting with Asn164 (TM4). Asn164 is a well-conserved residue within the POT family, with the equivalent position in $PepT_{St}$ and $PepT_{So2}$, forming a hydrogen bond to the peptide ligand (24, 25) (Fig. S5*C*). The result of this interaction in $PepT_{Xc}$ reduces the transport activity as truncation of the C terminus increases uptake (Fig. S5*D*). However, the interaction of the TEV sequence with the peptide binding site facilitated tighter packing in the unit cell and higher-resolution diffraction data to be collected. The peptide-binding site contains 31 water molecules, which can be clearly seen in the electron density maps (Fig. 4*B* and Fig. S6). A similarly solvated binding site was observed in the high-resolution crystal structures of GkPOT (23). However, unlike in GkPOT, we observe networks of hydrogen-bonded water molecules linking key protonatable side chains within the binding site. Specifically, we observe waters linking Asp322 and Glu425 ($PepT_{Xc}$ numbering, equivalent to Asp316 and Glu419 in $PepT_{So}$; Fig. 4*C*) and extending from the central peptide binding site to the conserved $E^{26}xxE^{29}$ RF motif on TM 1. Both of these sites are important for proton-coupled transport. The presence of ordered water networks linking them together provides a basis for the hypothesis that protons could move between different sites using the Grotthuss shuttling mechanism. Water networks in proteins have been studied via standard MD simulation, but only recently has the use of water as a mediator of proton movement been explicitly simulated for proton pumps (27), channels (28), and secondary active transporters (29, 30). We therefore sought to computationally investigate whether the water networks we observed could explicitly facilitate proton movement and play a similar role in the POT family.

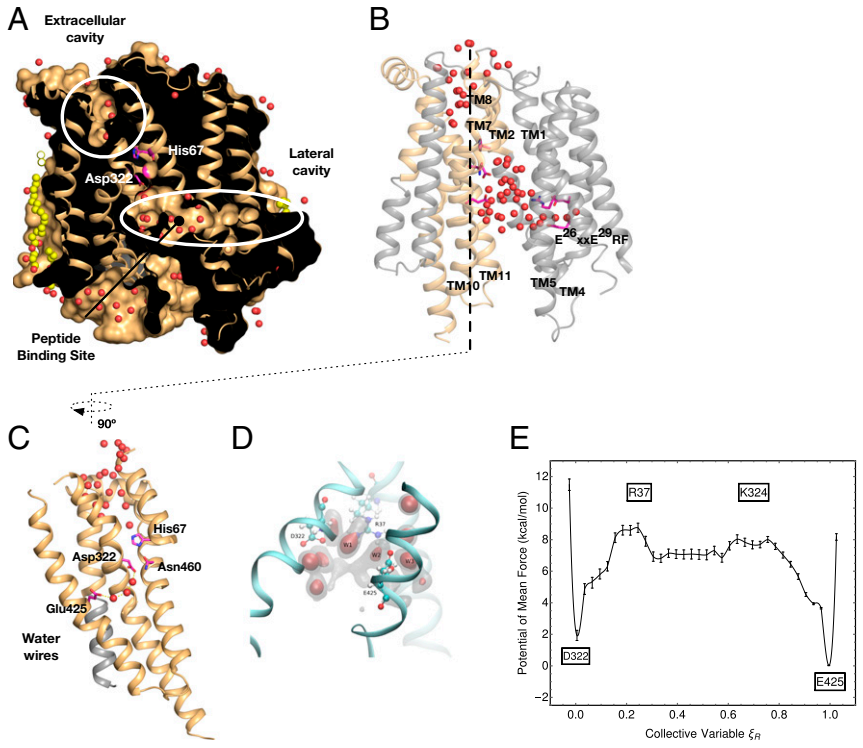

Fig. 4. Water networks connect proton binding sites within $PepT_{Xc}$. (*A*) Crystal structure of $PepT_{Xc}$ highlighting the observed extracellular and lateral cavities. Waters are shown as red spheres, bound lipid in yellow, and conserved histidine and aspartate residues in magenta. (*B*) Cartoon representation of $PepT_{Xc}$ indicating the waters seen in the crystal structure. (*C*) Water network observed from the extracellular cavity and the interactions observed within the conserved triad of aspartate, histidine, and asparagine residues. (*D*) Occupancy profile for water oxygens between Asp322 and Glu425 in $PepT_{Xc}$ averaged over 100 ns of the Glu425-protonated simulation. Regions where water oxygens exist over 40% of the time are shown in gray and regions with over 60% occupancy are shown in red. (*E*) Free energy profile (PMF) for proton transfer between Asp322 and Glu425. The reaction coordinates collective variable ξ_R transitions from zero when the Asp is protonated to one when the Glu is protonated. The positions of Asp322, Arg37, Lys324, and Glu425 are indicated by text boxes.

Water Wires Facilitate Proton Movement in the Binding Site. To probe the stability of the water in the high-resolution crystal structure, MD simulations were run on the $PepT_{Xc}$ protein embedded in a lipid bilayer composed of a 3:1 mixture of POPE (1-palmitoyl-2-oleoyl-*sn*-glycero-3-phosphoethanolamine) and POPG (1-palmitoyl-2-oleoyl-*sn*-glycero-3-phosphoglycerol) lipids, mimicking the experimental system. Standard protonation states were assigned for all residues other than Glu26 and Glu425, which were both protonated, based on PROPKA (31) calculations. The system reached equilibrium after 350 ns (rmsd 3.2 Å), with most of the changes occurring in the first 40 ns (rmsd 2.8 Å). Following equilibration, 100 ns of production simulation was collected. To inspect the solvation environment of Asp322 and Glu425, the water occupancy was analyzed in VMD (32) for this 100-ns trajectory. The result (Fig. 4*D*) shows that three water molecules (denoted as W1, W2, and W3) connecting Asp322 and Glu425 are stable over 60% of the time, which is consistent with those resolved in the crystal structure. A hydrogen bond analysis, using a distance criterion of 3.5 Å between oxygen atoms and an O–H–O angle criterion of 150°, showed that the two residues were connected by hydrogen-bonded water molecules 87.4% of the time. Thus, the waters in this region are very stable in the MD simulations.

Proton transport from Asp322 to Glu425 was then investigated with quantum mechanical/molecular mechanical (QM/MM) multiscale MD simulations combined with umbrella sampling (*Materials and Methods*) for the calculation of a free energy profile (i.e., potential of mean force, PMF). The PMF (Fig. 4*E*) shows that proton transport from Asp322 to Glu425 via the water molecules observed in the crystal structure is both thermodynamically favorable and kinetically feasible. When a proton is bonded to Glu425, the system is 1.9 kcal/mol lower in free energy than when Asp322 is protonated, suggesting an Asp-to-Glu proton transport direction, consistent with the movement of protons from the extracellular gate to the intracellular gate. The free energy barrier for this process is 6.8 ± 0.1 kcal/mol, resulting in a reaction rate of $177 \pm 40\ \mu s^{-1}$ based on transition state theory. The PMF additionally reveals two energy barriers along the reaction coordinate ($\xi_R = 0.2$ and $\xi_R = 0.7$) between Asp322 and Glu425. The positions of these barriers are close to the locations of Arg37 (TM1) and Lys324 (TM10), which is consistent with the expected influence of Coulomb repulsion between positively charged side chains and the positive charge of the excess proton. However, careful inspection of the umbrella sampling trajectories showed no proton disassociation from either Arg37 or Lys324, confirming that they do not directly participate in the proton transport. This is consistent with our transport data on the equivalent arginine in $PepT_{So}$ (Arg32) not being required for transport (Fig. 1*A*). These simulations thus verify that proton transport between Asp322 and Glu425 can be mediated by water and that it occurs on the microsecond timescale for the inward-open state of the system captured in the crystal structure.

Histidine Protonation Induces Inward- to Outward-Open Conformational Change. The histidine on TM2 (His57 human PepT1, His61 in $PepT_{So}$, and His67 in $PepT_{Xc}$) plays an important role in transport within the mammalian-like POT family members. In the crystal structures of both $PepT_{So}$ (Fig. 1) and $PepT_{Xc}$ (Fig. 4) it is situated at the base of a water-filled cavity that extends from the extracellular space down toward the extracellular gate. The formation of this cavity coupled with the close proximity of the histidine to water molecules suggests that histidine protonation may occur in the inward-facing state. This raises the question of whether protonation of this histidine has any implications for the transport mechanism. To further explore this question, MD simulations were initiated with His67 in $PepT_{Xc}$ protonated. Surprisingly, we observed a substantial conformational change within the extracellular gate region, resulting in the protein adopting an outward-facing state (Fig. 5 *A* and *B*) after only 450 ns of simulation. The simulations started from the inward-open crystal structure of $PepT_{Xc}$ in which His67 (TM2) is hydrogen-bonded to Ser326 (TM 8) and Asn460 (TM11). Asn460 is also hydrogen-bonded to Asp322 (TM7) (Fig. 5*C*). Upon protonation, the interactions of His67 with Ser326 and Asn460 are broken within 10 ns (Fig. S6). With the positional constraints on His67 and Asp322 (and thus the link between TM2 and TM7) loosened, the extracellular gate begins to open. A salt bridge is formed between His67 and Asp322, in agreement with the

functional link identified between these two residues (Fig. 3). The interacting time between His67 and Asp322 would likely be long enough to allow for proton movement between His67 and Asp322. However, after ~250 ns the His67–Asp322 salt bridge also becomes unstable as Arg37 (TM1) and Asn460 compete for interactions with Asp322. This allows TM1, 2 to move further away from TM7, 8, as demonstrated by the increasing distance between His67 and Ser326 (Fig. S7), thereby opening the extracellular gate to allow peptides access to the binding site. As the extracellular gate opens the intracellular gate helices, TM4, 5 and 10, 11 start to close, with conserved aromatic side chains packing together to constrict the exit pathway, as observed in $PepT_{St}$ (20).

Previously we and others have developed a method for determining the conformational state of an MFS transporter using the minimal helix tip distance between the extracellular and intracellular gate helices (19, 33). To assess the conformational state of the equilibrated MD ensemble of structures we constructed a similar 2D plot showing the current crystal structures of MFS members (Fig. 5*D*). The His67-protonated ensemble sits in the equivalent region of the plot occupied by YajR [Protein Data Bank (PDB) ID code 3WDO] and FucP (PDB ID code 3O7P), in their outward-open states. In contrast, simulation ensembles with neutral His67, with either Glu425 protonated or not, reside much closer to the presented inward-open crystal structure. Taken together the results of the MD analysis on $PepT_{Xc}$ suggest that proton binding to His67 in the inward-open state facilitates the reorientation of the transporter.

Concluding Remarks

An unusual biochemical property of the POT/PTR/NPF family is their ability to recognize diverse ligands while retaining a strict requirement to couple transport to the proton electrochemical gradient. We sought to investigate the proton coupling mechanism to discover whether differences exist between family members and to establish where such differences arise. Our results provide a number of insights. The first is that changes in the extracellular gate have a profound effect on the transport mechanism. They also identify a role for harnessing the potential energy of the proton gradient. Current models for proton-coupled symporters assume that protons bind before ligand when the transporter is already in the outward-open state, based on previous studies from LacY (34, 35). It is notable that the water cavity observed in both $PepT_{So}$ (19) and $PepT_{Xc}$ (this study) both extend toward the extracellular gate when the transporters are in inward-facing conformations. This structural feature would greatly facilitate the transfer of protons from the extracellular side of the membrane onto the histidine on TM2. The MD analysis demonstrates that proton binding at this site facilitates the spontaneous reorientation of the transporter from the inward-open to an outward-facing state (Fig. S8), thus influencing the reorientation step. The second finding supported by the multiscale QM/MM simulations is that ordered water networks are able to move protons via Grotthuss shuttling between the extracellular and intracellular gates. Our interpretation of this phenomenon is that the use of water to facilitate proton movement would allow proton coupling to be separated from ligand recognition and provide a plausible mechanism for protons to translocate between the extracellular and intracellular gates. Separating ligand recognition from proton movement would have clear advantages for accommodating chemically diverse ligands while retaining the ability to couple transport to the proton electrochemical gradient.

Materials and Methods

General Outline for Electrogeneic Transport Assays. Proteoliposomes were harvested and resuspended in the desired inside buffer (typically 10 mM Tris, pH 7.5, 2 mM $MgSO_4$, and 120 mM potassium acetate) and subjected to three rounds of freezing and thawing in liquid nitrogen and then extruded

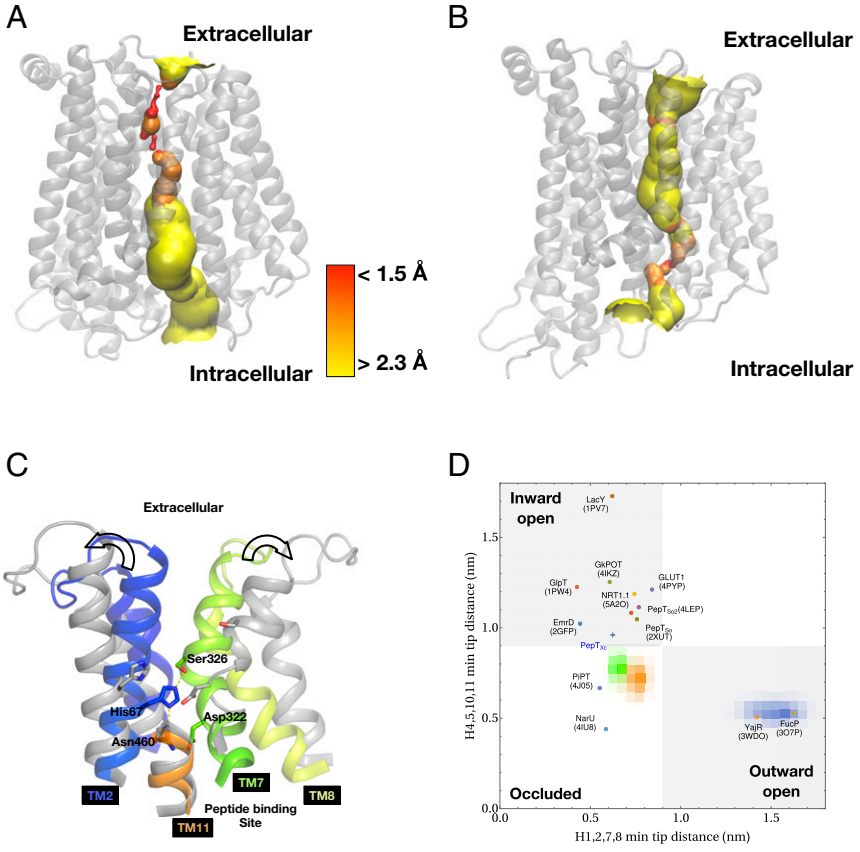

Fig. 5. Protonation of histidine on TM2 initiates inward- to outward-facing transition. Probe radius profiles for the crystal (*A*) and MD equilibrated structures (*B*) of $PepT_{Xc}$. The constriction along the transporting path is positioned at the extracellular gate in *A*, implying an inward-open state, while the constriction is positioned at the intracellular gate in *B*, implying an outward-open state. (*C*) Close-in view of the extracellular gate showing the conformational change following protonation of His67 from the crystal structure (colored) to MD equilibrated structure (gray). (*D*) Following protonation of His67, $PepT_{Xc}$ transitions from inward- to outward-facing conformation. The MD ensembles for His67-protonated (blue), Glu425-protonated (orange), and neither residue protonated (green) are compared with crystal structures of MFS transporters in different conformational states.

through a 0.4-μm membrane. The proteoliposomes were harvested and resuspended in a small volume of inside buffer. For the assays, 2 μL of proteoliposomes were diluted into 100 μL of external transport buffer (typically 10 mM Tris, pH 7.5, 2 mM $MgSO_4$, and 120 mM NaCl) containing a fixed amount of peptide with trace amounts of ^{3}H-labeled dialanine and incubated at 30 °C. This initiates transport through ΔpH produced by the acetate diffusion gradient (36, 37). To also impose a membrane potential (to generate delta $\Delta\mu H^+$) 1 μM valinomycin was added. After the desired length of time the reaction was stopped by filtering into 2 mL of water onto 0.2-μm nitrocellulose membranes; the membranes were washed twice before scintillation counting in Ultima Gold (PerkinElmer). The amount of substrate was calculated from a standard curve of the [^{3}H]dialanine; experiments were performed at least three times to generate an overall mean and SD. For details of specific experiments see *Supporting Information*.

Crystallization, Data Collection, and Processing. $PepT_{Xc}$ was purified to homogeneity and crystallized as described previously for $PepT_{So}$ in dodecyl maltoside (22). The final optimized conditions were 100 mM Tris·HCl, 120 mM ammonium tartrate, and 20% (vol/vol) PEG 400, pH 8.5. Data were collected on beamline I24 at Diamond Light Source. Data were integrated and scaled using the Xia2 pipeline to XDS and Aimless (Table S1). A molecular replacement search model was prepared from the crystal structure of $PepT_{So}$ (PDB ID code 4UVM). Initial phases were obtained by MR using Phaser. Iterative rounds of structure refinement were performed in Buster. The geometric quality of the model was assessed with MolProbity.

Classical and QM/MM MD Simulations. Classical MD simulations were run on the $PepT_{Xc}$ crystal structure embedded in solvated lipid bilayer mimicking the experimental system. Protonation states, if not specified above, were assigned based on PROPKA calculations. The CHARMM-CMAP and CHARMM 36 force fields were employed to describe the protein and lipid interactions, respectively. Two independent simulations (500 ns and 1.6 μs in length) were run in the GROMACS package, both demonstrating the same conformational transition. QM/MM simulations were initiated from an equilibrated structure with Glu425 protonated and performed in the CP2K package. The QM region was described by density functional theory (DFT) with the BLYP functional and the D3 dispersion correction. In some cases, multiscale reactive MD (MS-RMD) simulations were used to further equilibrate the system. The free energy profile for proton transport between Glu425 and Asp322 was then calculated with QM/MM umbrella sampling by tracking the center of excess charge (CEC) along a reaction coordinate (both defined in *Supporting Information*). The proton transport rate constant was then estimated using transition state theory. Full details on the simulations and calculations are provided in *Supporting Information*.

ACKNOWLEDGMENTS. We thank Dr. Christoph Wehmeye (Free University of Berlin) for helpful discussion on the error estimations in dTRAM; Dr. Dianfan Li, Dr. Syed T. A. Shah, and Dr. G. Kuteyi for assistance in crystallization and laboratory support; and Zhiyi Wu for assistance in liposome assays. This work was funded primarily through Wellcome Trust Investigator Award 102890/Z/13/Z (to S.N.). M.C. was supported by Science Foundation Ireland Grant 12/IA/1255. Research reported in this publication was also supported by the National Institute of General Medical Sciences, National Institutes of Health Grant R01GM053148 (to G.A.V., J.M.J.S., C.L., and Z.W.). The researchers used computing facilities provided by the Extreme Science and Engineering Discovery Environment, which is supported by National Science Foundation Grant OCI-1053575, as well as the University of Chicago Research Computing Center and the Texas Advanced Computing Center at the University of Texas at Austin.

1. Nakajima H, Hagting A, Kunji ER, Poolman B, Konings WN (1997) Cloning and functional expression in Escherichia coli of the gene encoding the di- and tripeptide transport protein of Lactobacillus helveticus. *Appl Environ Microbiol* 63:2213–2217.
2. Reddy VS, Shlykov MA, Castillo R, Sun EI, Saier MH, Jr (2012) The major facilitator superfamily (MFS) revisited. *FEBS J* 279:2022–2035.
3. Madej MG, Dang S, Yan N, Kaback HR (2013) Evolutionary mix-and-match with MFS transporters. *Proc Natl Acad Sci USA* 110:5870–5874.
4. Newstead S (2015) Molecular insights into proton coupled peptide transport in the PTR family of oligopeptide transporters. *Biochim Biophys Acta* 1850:488–499.
5. Léran S, et al. (2014) A unified nomenclature of NITRATE TRANSPORTER 1/PEPTIDE TRANSPORTER family members in plants. *Trends Plant Sci* 19:5–9.
6. Parker JL, Newstead S (2014) Molecular basis of nitrate uptake by the plant nitrate transporter NRT1.1. *Nature* 507:68–72.
7. Ito K, et al. (2013) Analysing the substrate multispecificity of a proton-coupled oligopeptide transporter using a dipeptide library. *Nat Commun* 4:2502.
8. Giacomini KM, et al.; International Transporter Consortium (2010) Membrane transporters in drug development. *Nat Rev Drug Discov* 9:215–236.
9. Rautio J, et al. (2008) Prodrugs: Design and clinical applications. *Nat Rev Drug Discov* 7:255–270.
10. Jardetzky O (1966) Simple allosteric model for membrane pumps. *Nature* 211:969–970.
11. Drew D, Boudker O (2016) Shared molecular mechanisms of membrane transporters. *Annu Rev Biochem* 85:543–572.
12. Newstead S (2017) Recent advances in understanding proton coupled peptide transport via the POT family. *Curr Opin Struct Biol* 45:17–24.
13. Parker JL, Mindell JA, Newstead S (2014) Thermodynamic evidence for a dual transport mechanism in a POT peptide transporter. *Elife* 3:e04273.
14. Smirnova IN, Kasho V, Kaback HR (2008) Protonation and sugar binding to LacY. *Proc Natl Acad Sci USA* 105:8896–8901.
15. Guan L, Kaback HR (2004) Binding affinity of lactose permease is not altered by the H+ electrochemical gradient. *Proc Natl Acad Sci USA* 101:12148–12152.
16. Andersson M, et al. (2012) Proton-coupled dynamics in lactose permease. *Structure* 20:1893–1904.
17. Kumar H, Finer-Moore JS, Kaback HR, Stroud RM (2015) Structure of LacY with an α-substituted galactoside: Connecting the binding site to the protonation site. *Proc Natl Acad Sci USA* 112:9004–9009.
18. Paulsen IT, Skurray RA (1994) The POT family of transport proteins. *Trends Biochem Sci* 19:404.
19. Fowler PW, et al. (2015) Gating topology of the proton-coupled oligopeptide symporters. *Structure* 23:290–301.
20. Solcan N, et al. (2012) Alternating access mechanism in the POT family of oligopeptide transporters. *EMBO J* 31:3411–3421.
21. Fei YJ, et al. (1997) Identification of the histidyl residue obligatory for the catalytic activity of the human H+/peptide cotransporters PEPT1 and PEPT2. *Biochemistry* 36:452–460.
22. Newstead S, et al. (2011) Crystal structure of a prokaryotic homologue of the mammalian oligopeptide-proton symporters, PepT1 and PepT2. *EMBO J* 30:417–426.
23. Doki S, et al. (2013) Structural basis for dynamic mechanism of proton-coupled symport by the peptide transporter POT. *Proc Natl Acad Sci USA* 110:11343–11348.
24. Guettou F, et al. (2014) Selectivity mechanism of a bacterial homolog of the human drug-peptide transporters PepT1 and PepT2. *Nat Struct Mol Biol* 21:728–731.
25. Lyons JA, et al. (2014) Structural basis for polyspecificity in the POT family of proton-coupled oligopeptide transporters. *EMBO Rep* 15:886–893.
26. Chen XZ, Steel A, Hediger MA (2000) Functional roles of histidine and tyrosine residues in the H(+)-peptide transporter PepT1. *Biochem Biophys Res Commun* 272:726–730.
27. Liang R, Swanson JM, Peng Y, Wikström M, Voth GA (2016) Multiscale simulations reveal key features of the proton-pumping mechanism in cytochrome c oxidase. *Proc Natl Acad Sci USA* 113:7420–7425.
28. Liang R, Li H, Swanson JM, Voth GA (2014) Multiscale simulation reveals a multifaceted mechanism of proton permeation through the influenza A M2 proton channel. *Proc Natl Acad Sci USA* 111:9396–9401.
29. Lee S, Swanson JM, Voth GA (2016) Multiscale simulations reveal key aspects of the proton transport mechanism in the ClC-ec1 antiporter. *Biophys J* 110:1334–1345.
30. Han W, Cheng RC, Maduke MC, Tajkhorshid E (2014) Water access points and hydration pathways in CLC H+/Cl- transporters. *Proc Natl Acad Sci USA* 111:1819–1824.
31. Olsson MHM, Søndergaard CR, Rostkowski M, Jensen JH (2011) PROPKA3: Consistent treatment of internal and surface residues in empirical pKa predictions. *J Chem Theory Comput* 7:525–537.
32. Humphrey W, Dalke A, Schulten K (1996) VMD: Visual molecular dynamics. *J Mol Graph* 14:33–38, 27–28.
33. Stelzl LS, Fowler PW, Sansom MS, Beckstein O (2014) Flexible gates generate occluded intermediates in the transport cycle of LacY. *J Mol Biol* 426:735–751.
34. Madej MG, Soro SN, Kaback HR (2012) Apo-intermediate in the transport cycle of lactose permease (LacY). *Proc Natl Acad Sci USA* 109:E2970–E2978.
35. Kaczorowski GJ, Kaback HR (1979) Mechanism of lactose translocation in membrane vesicles from Escherichia coli. 1. Effect of pH on efflux, exchange, and counterflow. *Biochemistry* 18:3691–3697.
36. Lancaster JR, Jr, Hinkle PC (1977) Studies of the beta-galactoside transporter in inverted membrane vesicles of Escherichia coli. II. Symmetrical binding of a dansylgalactoside induced by an electrochemical proton gradient and by lactose efflux. *J Biol Chem* 252:7662–7666.
37. Kaczorowski GJ, Robertson DE, Kaback HR (1979) Mechanism of lactose translocation in membrane vesicles from Escherichia coli. 2. Effect of imposed delta psi, delta pH, and delta mu H+. *Biochemistry* 18:3697–3704.
38. Lancaster JR, Jr, Hinkle PC (1977) Studies of the beta-galactoside transporter in inverted membrane vesicles of Escherichia coli. I. Symmetrical facilitated diffusion and proton gradient-coupled transport. *J Biol Chem* 252:7657–7661.
39. Grimme S, Antony J, Ehrlich S, Krieg H (2010) A consistent and accurate ab initio parametrization of density functional dispersion correction (DFT-D) for the 94 elements H-Pu. *J Chem Phys* 132:154104.
40. Chandler D (1987) *Introduction to Modern Statistical Mechanics* (Oxford Univ Press, New York), p 274.